PCCP

PAPER

View Article Online
View Journal | View Issue

Cite this: *Phys. Chem. Chem. Phys.*, 2025, **27**, 21244

Doubly ionised 2,4-imidazolidinedione (hydantoin) dissociations induced by electron collision, fragmentation thresholds *vs.* vertical excitation energies

P. Moretto-Capelle,[a] A. Scemama,[b] S. Faure,[a] E. Dudás,[a] P. Cafarelli[a] and J.-P. Champeaux *[a]

Received 28th April 2025,
Accepted 9th September 2025

DOI: 10.1039/d5cp01613d

rsc.li/pccp

The double ionisation/dissociation process for a prebiotic molecule (hydantoin) induced by 20–40 eV electron collisions was studied using time-of-flight spectrometry and velocity map imaging. Fragmentation into two molecular cations reveals that hydrogen transfer occurs in the excited state. Furthermore, the thresholds of the main dissociation channels were measured. Comparison with state-of-the-art calculations of the vertical excited states of hydantoin^{2+} gives an accurate indication of the initial population of the excited states.

1 Introduction

The hydantoin molecule is a prebiotic molecule, a chemical precursor that could be a key to the origin of life on Earth, and the subject of our previous studies of singly charged cation dissociation.[1] It is known to exist in extraterrestrial environments thanks to detection in samples from two meteorites: Murchinson and Yamato-7191198. Pathways to its formation were identified in De Marcellus *et al.* which showed that UV photon irradiation of interstellar ice analogues containing small molecules such as H_2O, CH_3OH, and NH_3 can lead to the production of numerous molecules, including hydantoin.[2,3]

Organic molecules like hydantoin can be irradiated by energetic UV photons as well as collide with charged particles (electrons, ions) from stellar winds, resulting in electron excitation and ionisation processes. This raises the possibility of forming small carbon-containing dications when the molecular system relaxes. Molecular dications have been found in notable concentrations in astrophysical environments such as the ionospheres of planets, in particular CO_2^{2+} and N_2^{2+} in the ionospheres of Mars, Venus and Titan.[4] Those dications are highly reactive[5] and can participate in the formation of large aromatic compounds through chemical reaction with acetylene or benzene, for example.[6]

One of the special features of these small molecular dictations like CO_2^{2+} is their metastability due to a potential barrier to dissociation in the potential energy curve of their ground state.[7,8] Dissociation processes of such dications lead to charge separation where two monocations are formed (and potentially neutral fragments).[9] Because of coulombic repulsion between charges, "high" kinetic energy release (1–5 eV) is shared between ionic dissociative products. In the case of atmospheric doubly charged ions, this kinetic energy can be larger than escape energy of the atmosphere as shown in Lilenstein *et al.*[4] Our experimental study of the interaction of multicharged ions (minority species in the solar wind) at 'low' energy (keV u^{-1}) on the hydantoin molecule[10] has enabled us to highlight the molecular fragmentation patterns induced, as well as the relatively high charge states (2^+ and the unstable 3^+) reached by the molecule and favoured by "soft" electron capture processes on the multicharged projectile.

Although many fragments were observed, the energetic part of the dissociation processes was not accessible. Fragmentation thresholds can be obtained either by photon interaction thanks to synchrotron radiation[11,12] or by electron collision.[13] In this paper, we present our new results on double ionisation of hydantoin molecule and propose an analysis of the corresponding fragmentation patterns induced by electron collision in the 20–40 eV energy range.

2 Experimental procedures

The experimental set-up (named SWEET) has already been described in Champeaux *et al.*[1] Briefly, a pulsed bunch of electrons of a given energy (≈100–1000 e$^-$ per bunch) with very low temporal width of ≈1 ns collides with a low density, collimated (2 mm width), and continuous jet of neutral

[a] *Laboratoire Collisions Agregats et reactivité, University of Toulouse, UMR 5589-CNRS, Toulouse, France. E-mail: jean-philippe.champeaux@irsamc.ups-tlse.fr*
[b] *Lab. de Chimie et Physique Quantiques, University of Toulouse, Toulouse, France*

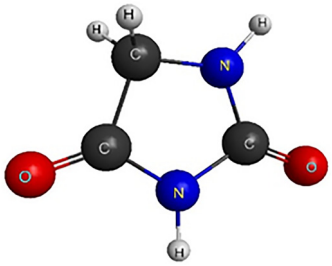

Fig. 1 Neutral hydantoin molecule.

hydantoin molecules (Fig. 1) (98% purity, purchased form Sigma Aldrich) produced by an oven heated at 150 °C inside a vacuum chamber at 10^{-7} torr.

For each collision between one electron of the bunch and one molecule of the jet, two cationic fragments are created after double ionisation of the hydantoin molecule. The fragments were mass-to-charge ratio (m/z) and velocity analysed by our home-made pulsed time-of-flight mass spectrometer and velocity map imaging setup (TOF-VMI).

Synchronisation between the electron bunch and TOF-VMI extraction is key especially when considering the production of two cationic fragments with a high kinetic energy due to the coulombic repulsion between them. Therefore, the delay between the extraction pulse of the TOF-VMI and the triggering of the electron pulse must be chosen so that:

(i) The electron packet can pass through the extraction cell without being disturbed.

(ii) The ions created by the collision don't have much time to move, otherwise the resolution and detection efficiency will be reduced.

In this experiment a delay of about 100 ns was used, which for 10 eV electrons corresponds to a distance travelled of 19 cm (*i.e.* 8 cm after the extraction cell). Carbon ions with an energy of 4 eV (upper value) created by the collision will travel 400 μm, given the geometry of our system, which is negligible.

The period of bunches must be larger than the maximum time of flight we wish to record (heaviest mass) to avoid overlap of mass spectra. Typically for 40 eV electrons, the working frequency was $f \approx 20$ kHz. The VMI-TOF detector was a multi-channel plate (MCP, diameter 40 mm). Impact position (X, Y) on the MCP was obtained thanks to a two-dimensional delay line anode developed by Roentdek.[14] The four anode signals were amplified by four timing preamplifiers (VT120, Ortec), processed by an 8-channel constant fraction discriminator (CF8000, Ortec) and were fed to a 16 channel time to digit convertor (TDC developed by DTPI, LUMAT, Orsay[15]) with a 120 ps time step triggered by the electron pulse command.

Each event (with four timing signals for each detected fragment) was stored (list-mode) for further analysis. The time of flight (TOF, which is related to the mass-to-charge ratio) between the extraction pulse and the MCP detection as well as t MCP impact coordinates (X and Y, related to the fragment momentum) were recorded for each fragment. We determined the three-dimensional velocity vector for each detected charged fragment for each collision event through the following relations:

$$\begin{cases} v_x = \dfrac{X}{\mathrm{TOF}} \\ v_y = \dfrac{Y}{\mathrm{TOF}} \\ v_z = -\dfrac{qE}{m}(\mathrm{TOF} - T_0) \end{cases} \quad (1)$$

T_0 is the TOF of the fragment with mass m without any initial velocity *i.e.* the centre of the TOF peak for a given mass m, q is the charge of the fragment and E is the extracting field.

In this work, the incident electron energy was tuned from 20 to 40 eV with a 0.5 eV step (which is close to the average resolution of the electron gun). The electron energy was calibrated by injecting helium gas as the target and measuring its ionisation potential (24.58 eV[18]).

In the case of double ionisation of hydantoin by electron impact, the resulting dication has the same geometry as the ground state of the neutral. It is generally electronically excited (vertical transition), non-stable, and dissociates into two charged fragments (A^+, B^+) and possibly other neutral fragments $\{X^0\}$ *via* the following reactions:

$$\mathrm{Hyd}^0 + e^- \rightarrow \mathrm{Hyd}^{2+*} + 3e^- \quad (2)$$

$$\searrow A^+ + B^+ + \{X^0\}$$

For each event of this kind at a fixed electron energy, the TOF of A^+ and B^+ were recorded ($\mathrm{TOF_A}$ and $\mathrm{TOF_B}$). Adding event-by-event contributions, the two-dimensional correlation map was then obtained by counting ($\mathrm{TOF_A}$, $\mathrm{TOF_B}$) couples *i.e.* $n_{\mathrm{count}} = f(\mathrm{TOF_A}, \mathrm{TOF_B})$. In such a correlation map (see Fig. 4) islands appear corresponding to a specific dissociation of the parent molecule into two specific cations.

Then, by recording the number counts of an A^+/B^+ correlation island as a function of electron energy, we can determine the appearance energy threshold of this specific dissociation channel. Because the data acquisition was realised in event-by-event pulsed mode, 3D velocity components, as well as the total kinetic energy, were directly calculated for each of the detected correlated charged fragments (A^+/B^+). The complete determination of the 3D velocity vector eliminates the need for Abel inversion modelling (in the case of the v_x, v_y. components and continuous recording)[16] or TOF profile reconstruction (in case of the v_z component) using pre-calculated basis functions.[17]

3 Theoretical investigations

Two types of calculation have been performed for this work on the hydantoin dication: some dissociation limits and determinations excited states vertical energies.

3.1 Neutral hydantoin geometry and dissociation limits

Evaluation of geometry of the neutral molecule and corresponding energy as well as dissociation limits calculations have

been done using GAMESS code[19] using the 6-311G(d,p)** basis set. For a given dissociation limit, each geometry of the fragment is optimised taking into account the molecular charge.

Coulombic repulsion occurs between charged fragments. This causes a variation in the molecular energy level with respect to $1/R$, where R is the distance between cations. This explains the kinetic energy release of several eV in the dissociation process, as well as the fragmentation threshold being much higher than the dissociation limit. Results are given in Fig. 8 relative to the ground state of the neutral hydantoin molecule, which is the natural reference for the kinetic energy of the incoming electron.

3.2 Excited states of hydantoin dication

To investigate the electronic states of the hydantoin dication Hyd^{2+}, we employed the equation-of-motion double ionisation potential coupled-cluster singles and doubles method with three-hole one-particle operators (EOM-DIP-CCSD(3h-1p)).[20–22] This computational approach was specifically designed to predict the energy levels of systems following the removal of two electrons and is implemented in the Q-Chem software.[23] In this method, the reference state (neutral hydantoin) is described using coupled-cluster theory with single and double excitations (CCSD), which efficiently accounts for electron correlation effects. The EOM extension gives information on the doubly ionised states by solving for the eigenvalues of the correlated Hamiltonian within the subspace corresponding to configurations with two electrons removed. This approach is often reported to provide a favourable compromise between computational cost and accuracy, with typical error estimates in the range of 0.1–0.3 eV for energy gaps with small basis sets.[24] A recent benchmark using the aug-cc-pVTZ basis set indicates higher errors, with a mean signed error (MSE) of 0.61 eV observed for a set of 23 molecules.[25]

The geometry of hydantoin was first optimised at the B3LYP/6-311G(dp)** level. EOM-DIP-CCSD(3h-1p) calculations were then carried out with both the aug-cc-pVDZ and aug-cc-pVTZ basis sets. We observed that increasing the basis set size did not alter the ordering of the ionised states, and that the energy differences remain consistent between the two basis sets to within 0.1 eV.

However, due to the truncation of excitation operators in the method, electron correlation effects are generally described more accurately in the neutral reference than in the doubly ionised states. This discrepancy accounts for the overall shift of +0.4 eV in the spectrum when the larger basis set was employed.

Assuming that the ionised states are uniformly well described, we proceeded to compute the energies of the neutral ground state and the doubly-ionised triplet ground state at the CCSD(T)/aug-cc-pVTZ level. We then applied a shift of −0.56 eV to the EOM-DIP-CCSD(3h-1p)/aug-cc-pVTZ energies of the ionised states, aligning the double ionisation energy of the lowest triplet state with the corresponding CCSD(T) value. The results are reported in Table 1.

The required −0.56 eV correction in the large basis set is in excellent agreement with the +0.61 eV MSE reported in ref. 23 for the same basis. Moreover, due to error compensation, the excitation energies obtained with the smaller aug-cc-pVDZ basis set deviate by less than 0.3 eV from our corrected values, in agreement with.[24] These results confirm that the EOM-DIP-CCSD(3h-1p)/aug-cc-pVDZ method may be employed for similar larger molecules without necessarily requiring a correction.

Table 1 Excitation energies (eV) of singlet and triplet states with symmetry A′ and A″ in the 26–32 eV energy range computed with the EOM-DIP-CCSD(3h-1p) method with the aug-cc-pVDZ and aug-cc-pVTZ basis sets. The aug-cc-pVTZ values are corrected to match the CCSD(T)/aug-cc-pVTZ singlet–triplet energy difference. Dipole moments (Debye) are also reported

	aug-cc-pVDZ	aug-cc-pVTZ	Corrected	
State	Exc. energy (eV)	Exc. energy (eV)	Exc. energy (eV)	Dipole moments (Debye)
Neutral				2.92
1A′	26.6218	27.0708	26.51	0.27
	27.2171	27.6607	27.10	3.41
	28.5444	28.9653	28.41	4.88
	30.2428	30.6517	30.09	2.80
	30.8245	31.2315	30.67	3.72
	30.8869	31.2784	30.72	1.28
	31.2295	31.6060	31.05	0.57
	31.5673	31.9708	31.41	6.31
	32.1791	32.5620	32.00	4.21
1A″	26.2679	26.7259	26.17	4.24
	27.4037	27.8439	27.29	3.63
	28.6612	29.0955	28.54	4.35
	29.4885	29.9069	29.35	5.90
	30.7815	31.1894	30.63	3.51
	31.0306	31.4107	30.85	4.37
	31.5256	31.9250	31.37	3.54
	31.7039	32.0847	31.53	3.36
	32.4211	32.7950	32.24	4.50
3A′	26.6867	27.1334	26.58	0.25
	26.7880	27.2351	26.68	3.12
	30.1610	30.5627	30.00	4.17
	30.9623	31.3396	30.78	2.37
	31.0163	31.3959	30.84	0.64
	31.3092	31.6809	31.12	0.64
	31.5970	31.9902	31.43	4.48
	31.7614	32.1344	31.58	4.26
	32.2838	32.6613	32.10	3.19
3A″	26.2493	26.7088	26.15	4.24
	27.3309	27.7779	27.22	3.48
	28.4545	28.9050	28.35	4.48
	29.1886	29.6319	29.07	6.31
	30.7270	31.1385	30.58	3.59
	31.0167	31.3969	30.84	4.53
	31.4247	31.8322	31.27	4.49
	31.6936	32.0719	31.51	4.06
	32.3608	32.7366	32.18	4.92

This new theoretical investigation with higher precision gives a vertical double ionisation potential of 26.15 eV (^{3}A″)–26.17 eV (^{1}A″), about 1 eV lower than the 27.1 eV previously reported.[10]

4 Results and discussions

4.1 In search of unfragmented dication

The unfragmented hydantoin (100 u) dication (Hyd^{2+}) is expected to appear in a single-cationic event detection spectrum at m/z = 50 for an electron projectile with energy above the

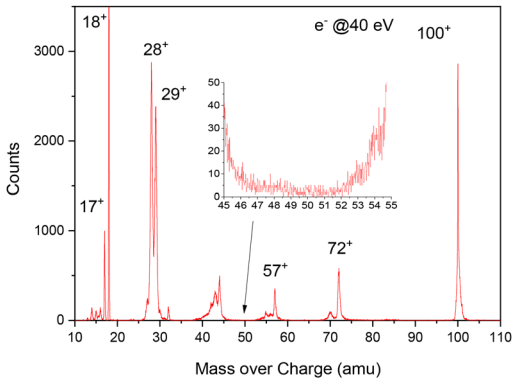

Fig. 2 Cationic mass spectrum from single ionisation hydantoin events at 40 eV incident electron energy.

theoretical vertical double ionisation threshold of the molecule at 26.1 eV (see ref. 10). Experimentally, no signal is observed as shown in the zoom of Fig. 2. If the unfragmented dication exists, its lifetime, after 40 eV e^- excitation energy, is therefore much lower than the 900 ns corresponding to our VMI acceleration zone.

In previous work[10] unfragmented Hyd^{2+} was observed (only as a trace) in keV O^{6+} collisions but not with keV He^{2+} as the projectile. These results suggest that for electron projectiles (as well as He^{2+} projectiles), the electronic excitation process follows the ionisation path and results systematically in the dissociation of the molecule.

This was not the case with O^{6+} ions, where "cold" charge transfer from the projectile ($O^{6+} \rightarrow O^{5+}$) could occur with no or low energy transfer. We can therefore infer that a very low energetic barrier exists (which can be easily overcome) between stable doubly ionised hydantoin and the dissociative pathways of the molecule.

This hypothesis is reinforced by a DFT-B3LYP calculation of the stable relaxed geometry of Hyd^{2+}, as shown in Fig. 3, where major geometry change is observed compared to the neutral.

As previously discussed in ref. 10, Hyd^{2+} presents (in the ground state) a barrier-less opening of the hydantoin ring between the $C^{(4)}$–$C^{(5)}$ carbon bond, forming a chain that exhibits weak bonds: $C^{(4)}$–$N^{(3)}$, $N^{(3)}$–$C^{(2)}$, $C^{(2)}$–$N^{(1)}$, and $N^{(1)}$–$C^{(5)}$. The huge gap (−4.4 eV) calculated between vertical double ionisation threshold and the Hyd^{2+} relaxed geometry could induce further modifications due to conversion into internal energy. Dynamical reaction coordinates calculations didn't show any further strong geometrical modifications besides ring opening.

A combination of the possibility of a low barrier to dissociation advocates for high dication instability.

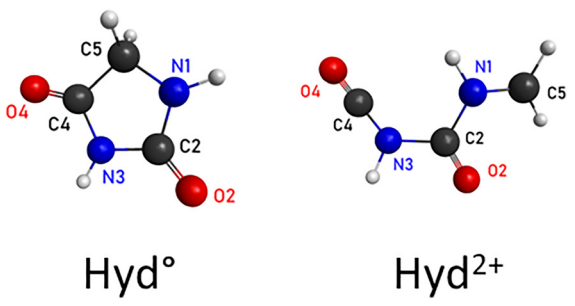

Fig. 3 Relaxed geometries of neutral and doubly ionised hydantoin calculated using 6-311G(d,p)** basis and DFT-B3LYP method. The Hyd^{2+} minima corresponding to the presented geometry lies at −4.4 eV from vertical double ionisation potential of the molecule.

4.2 Dicationic correlation map analysis

The raw correlation map recorded for an incident electron energy of 40 eV (*i.e.* far above the double ionisation threshold of the hydantoin molecule, to ensure that the maximum number of dissociative channels are open) is shown in Fig. 4.

The vertical bands observed in the correlation map (highlighted in yellow in Fig. 4) correspond to non-correlated events and are removed for data analysis as described in Section 4.3.1. They correspond to false correlations coming from two single ionisation processes created by two different electrons belonging to the same pulse.

Only four dissociation channels are clearly observed even though the excitation energy (40 eV) is more than 10 eV over the double ionisation threshold of hydantoin. The two masses involved in the correlation island are simply determined by the two TOF values of the centre of the island. Branching ratios of the observed dissociation channels are presented in Table 2. The most intense dissociation leads to a $28^+/43^+$ (+29) u correlation island.

The shape of the correlation island reflects the correlated momenta projection components of the two cations over the axis of the TOF cell.[26] Measured island slopes are presented in Table 2. A "−1" slope indicates that dissociation follows a two-body dissociation after (if any) low velocity initial neutral emission:

$$Hyd^{2+} \rightarrow AB^{2+} + \{X^0\} \rightarrow A^+ + B^+ + \{X^0\} \quad (3)$$

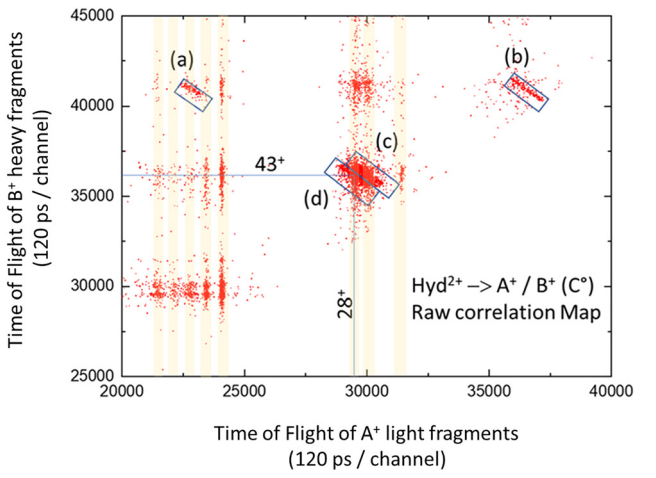

Fig. 4 Two-dimensional time-of-flight correlation spectrum corresponding to the dissociation of the dication at 40 eV incident electron energy: (a) m/z = {16, 56}; (b) m/z = {44, 56}; (c) m/z = {29, 43}; (d) m/z = {28, 43}.

Table 2 Branching ratio of A^+/B^+ fragmentations channels measured at 40 eV incident electrons and slope. Numbers in brackets refer to yields measured at 100 eV

Mass (u)	Branching ratio (%) 40 eV	Slope	Dissociation mechanism
(a) $16^+/56^+$ (28°)	7 (3.9)	−0.64	Initial charge separation
(b) $44^+/56^+$	12 (6)	−1	Charge separation
(c) $29^+/43^+$ (28°)	34 (28.8)	−1	Neutral then charge separation
(d) $28^+/43^+$ (29°)	47 (61.2)	−1	Neutral then charge separation

This case corresponds to the (b), (c), and (d) dissociations. A non "−1" slope the (a) case—indicates an initial charge separation followed by neutral emission(s) from one of the two cation fragments (or both) as follows:

$$Hyd^{2+} \rightarrow (AX)^+ + B^+ \quad \text{or} \quad A^+ + (BX)^+ \rightarrow A^+ + B^+ + \{X^0\} \qquad (4)$$

It is worth noting that breaking one (or sequentially two) molecular bounds from the Hyd° ring geometry or the Hyd^{2+} open geometry leads easily to the observed cationic fragments masses in the correlation map without any strong molecular rearrangement. For example: 43 (HNCO), 28 (CO), and 29 ($HNCH_2$) as shown in Fig. 5.

In the case of rapid charge separation (coulombic-like repulsion with high fragmentation kinetic energy) we expect that the molecule does not have time to change geometrical conformation before dissociation so, the produced cations may be formed considering an initial atom arrangement close to the neutral geometry of the molecule.

Correlation island (b) clearly shows hydrogen transfer within the molecule, resulting in the fragmentation of two bodies without a neutral particle. Island (a) also corresponds to a hydrogen transfer, but the dissociation process is more complex as it involves the emission of a neutral particle.

While mass 44 can be attributed to the HNCOH or H_2NCO isomers, the complementary part could correspond to several isomers. As we do not have experimental access to the molecular reaction dynamics, it is difficult to definitively attribute the geometry of the observed masses in the correlation map.

Generally, further in-depth theoretical studies are required to determine the most likely pathways, which depend on which initial excited state is populated (see Fig. 8). This is beyond the scope of this article as it involves molecular dynamics in excited states, including the possibility of conical intersections.

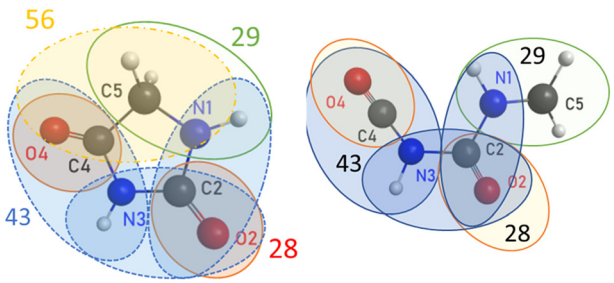

Fig. 5 Example of the 43, 28, and 29 parts of Hyd° and Hyd^{2+}.

Some of the reaction paths have been calculated in ref. 10, but these were based only on the ground state (open geometry) of the Hyd^{2+} ion.

4.3 Measurements of dicationic fragmentation thresholds

For a given excited electronic state initial population, a dissociation channel can then be opened and produce specific A^+/B^+ correlated pairs (with neutral(s)) as displayed in the correlation map presented in Section 4.2. Examination of the total intensity of A^+/B^+ correlation pairs, as a function of incident electron energy, gives specific dissociation energy thresholds in relation to the energy of the corresponding excited electronic state. However, while the measurement of electron-induced ionisation and/or fragmentation thresholds is easily determined for (initially) singly charged molecules, such information is much more difficult to obtain for di-cations since:

(i) Multi-stop (*i.e.* correlated spectroscopy), event-by-event detection must be available.

(ii) The effective cross-section of double ionisation by electron impact on the molecule is very small compared to single ionisation: for 40 eV electrons, over 90% of the measured signal corresponds to single ionisation. Signal accumulation must therefore benefit from very good experimental stability over several days to obtain sufficiently good statistical data.

(iii) The correlated events associated with the formation of two cations are contaminated by false, fortuitous events arising from the formation of two cations from two different molecules, induced by two electrons from the same bunch. This is true even for good experimental conditions: typically, 100–1000 e^- per bunch and a low density effusive molecular jet in the SWEET experiment.

Therefore, a compromise must be found to ensure a sufficient count rate but without having too many fortuitous events, so that they can be corrected and do not mask the truly correlated signal.

4.3.1 Fortuitous events corrections. Let us consider a pulse containing N electrons. Assuming a low-density molecular jet of density ρ and an overlap length L between the molecular jet and the electron beam, so that the unique collision condition is fulfilled, we can relate the collisional probability to the collisional cross section:

$$P_r = \rho\sigma_t L \qquad (5)$$

Then, the probability that any reaction occurs for an electron pulse (containing N-electrons) is given by:

$$P_{reac} = 1 - (1 - P_r)^N \qquad (6)$$

The probability that only one reaction occurs (P_{single}) is:

$$P_{single} = C_1^N P_{reac}(1 - P_{reac})^{N-1} = NP_{reac}(1 - P_{reac})^{N-1} \qquad (7)$$

In the same way, the probability that two reactions occur is:

$$P_{double} = C_2^N P_{reac}{}^2(1 - P_{reac})^{N-2}$$

or

$$P_{double} = \frac{N(N-1)}{2} P_{reac}{}^2(1 - P_{reac})^{N-2} \qquad (8)$$

The probability ratio between one single e^- per molecule interaction and 2 different interactions per pulse is given by:

$$\frac{P_{\text{double}}}{P_{\text{single}}} = \frac{P_{\text{reac}}(N-1)}{2(1-P_{\text{reac}})} \quad (9)$$

Two cations (A^+ and B^+) can be formed either by a one e^- collision event causing double ionisation (*i.e.* producing Hyd^{2+}) followed by a dissociation leading to an A^+/B^+ correlated fragment pair with a cross section σ_{AB} (a non-fortuitous correlated event), or, in case of fortuitous events, by two different single ionisation events of two different electrons colliding with two different molecules with each one forming cations A^+ and B^+ with non-correlated cross sections σ_A and, respectively, σ_B.

The probability π_{nf} of a non-fortuitous (nf) event is then:

$$\pi_{nf} = P_{\text{single}}\rho L\sigma_{AB} \quad (10)$$

and the probability π_f of a fortuitous event is:

$$\pi_f = P_{\text{double}}(\rho L\sigma_A)(\rho L\sigma_B) \quad (11)$$

The probability ratio between fortuitous and non-fortuitous correlation is then:

$$\frac{\pi_f}{\pi_{nf}} = \frac{P_{\text{reac}}(N-1)}{2(1-P_{\text{reac}})}\rho L \times \frac{\sigma_A\sigma_B}{\sigma_{AB}} \quad (12)$$

We observed, as expected, that the probability of fortuitous events grows with the density of molecules and the number N of electrons and is proportional to σ_A and σ_B.

Now after k electron pulses of N electrons per pulse each, we experimentally record a total of Γ_{tot} counts in an A/B correlation island of the correlation map. Γ_{tot} can then be written as:

$$\Gamma_{tot} = k\pi_f + k\pi_{nf} \quad (13)$$

Naming N_A and N_B the number of fortuitous A^+ and B^+ in the island, and N_{AB} the number of good correlations so that

$$\begin{aligned} N_A &= k(P_{\text{reac}}\rho L\sigma_A) \\ N_B &= k(P_{\text{reac}}\rho L\sigma_B) \end{aligned} \quad (14)$$

and $N_{AB} = k\pi_{nf}$.

We can then rewrite the total number of counts in a correlation island Γ_{tot} as function of N_A, N_B and N_{AB}:

$$\Gamma_{tot} = \frac{N(N-1)(1-P_{\text{reac}})^{N-2}}{2k}N_AN_B + N_{AB}$$

which can be written as:

$$\Gamma_{tot} = \alpha N_AN_B + N_{AB} \quad (15)$$

To estimate α we must choose a two-dimensional region of interest (ROI) of the correlation map where we are sure that counts are proceed only by purely fortuitous events. There are cases, for example the A^+/Hyd^+ signal, which cannot derive from one single collision event. For these particular ROIs, N_{AB} is obviously null and from eqn (15) we have:

$$\alpha = \left(\frac{\Gamma_{tot}}{N_AN_B}\right)_{\text{in ROI}} \quad (16)$$

As we record every signal from particular 1-stop events forming independently A^+ or B^+ from Hyd^+ (with the same probability to occur as a fortuitous count), we can calculate N_A and N_B in the chosen ROI, and, by extension, α.

Finally, considering a correlation island, for example (a): $16^+/56^+$ (28°), containing Γ_{tot} counts and having N_{16^+} and N_{56^+} counts from single ionisation events, the "real" non fortuitous correlation $16^+/56^+$ counts from the Hyd^{2+} map are calculated using (15) and (16).

4.3.2 Procedure for determining the position of dissociation thresholds. The evolution curve $N(E_e)$ of the intensity of a fortuitously-corrected correlation island (see Section 4.3.1) as a function of the excess energy is fitted by a Wannier[27] power law:

$$N(E_e) = N_c + N_0 \cdot H(E_e - E_{\text{threshold}})(E_e - E_{\text{threshold}})^a \quad (17)$$

where N_c is the background signal (noise level before threshold), $E_{\text{threshold}}$ the desired dissociation threshold energy, N_0 and a are fitting parameters and $H(x)$ is the Heaviside distribution. Denifl *et al.*[13] have successfully applied this law (derived from atomic physics) to fragmentation process. A complete discussion of the extension of this law to polyatomic molecules can be found in ref. 28.

The uncertainties for the energy appearance measurements presented in this article are evaluated by considering the measured thermal emission energy width of the electron gun (0.15 eV), combined with the uncertainties arising from the curve fitting procedure using eqn (17). The statistical uncertainty of each measured data points in the curve fitting is accounted for by assuming it is proportional to the square root of the number of counts. The overall uncertainty is then determined by combining these two uncertainties. The final total uncertainty is then rounded to the upper first decimal.

4.3.3 Appearance energies of $44^+/56^+$ and $16^+/56^+$ (28°) correlations. The signal curves $N(E_e)$ of these two correlation islands are presented in Fig. 6, with their analytic expressions:

The two thresholds are very close, measured at 28.6 ± 0.3 eV and 28.7 ± 0.3 eV.

They are 2.4 eV higher than the calculated double ionisation potential of Hyd. Both lead to a 56^+ u cation.

The two-body $44^+/56^+$ fragmentation, already seen in ref. 10, correlated to excitation of the dication,[29] as well as the $16^+/56^+$ correlation (correlated to a neutral emission of mass 28), show a clear signature of hydrogen transfer in excited state (ESHT).

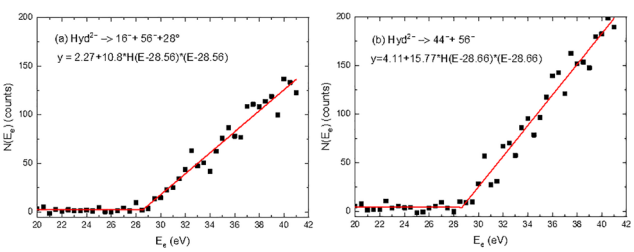

Fig. 6 Intensity evolution of (a) $16^+/56^+$ and (b) $44^+/56^+$ correlations *vs.* electron energy.

4.3.4 Appearance energies of the $29^+/43^+$ (28°) and $28^+/43^+$ (29°) correlations. For these correlations, the appearance energy threshold is more difficult to obtain. This is due to a significant population of the 28 u and 29 u cations produced after single ionisation of the molecule causing a strong fortuitous contamination in the correlation map, as shown in Section 4.2 (vertical bands highlighted in yellow). Moreover, the two correlation islands are difficult to discriminate because only one mass unit separates the light cations, meaning that correlation islands can overlap. To obtain the (c) and (d) appearance energies, we employed two different methods.

First, we use two rectangular boxes to define the ROI around the correlation islands without overlap, like for the (a) and (b) cases (see Fig. 4). Corresponding intensities in the ROI of the $29^+/43^+$ and $28^+/43^+$ signals as a function of electron energy is presented in Fig. 7. With this method we measure 29.4 ± 0.3 eV for the $29^+/43^+$ dissociation and 30.1 ± 0.3 eV for the $28^+/43^+$ dissociation. For the $28^+/43^+$ case we notice that a second slope rupture seems to appear at higher energy than the previous threshold, with a corresponding energy estimated at 35.2 eV. Further investigations are needed to confirm this second threshold.

Secondly, we only used the wings of the correlation islands because of less contamination here by fortuitous events. With this approach, we measure 30.1 ± 0.3 eV for $29^+/43^+$ and 31.1 ± 0.3 eV for $28^+/43^+$. Finally, we average the two determinations of the dissociation energies to give 29.7 ± 0.5 eV and 30.6 ± 0.5 eV for the $29^+/43^+$ and $28^+/43^+$ correlations respectively.

In panel (Fig. 7c and d), a small increase in the baseline is observed around 22 eV. However, this threshold-like feature is likely an artifact. Since it appears 4 eV below the vertical double-ionization threshold of the molecule (26.1 eV, ref. 10), it cannot be clearly attributed to a genuine $28^+(29^+)/43^+/29°(28°)$ correlation originating from the doubly ionized Hydantoin molecule. While such a process—producing two correlated charged fragments below the double-ionization threshold—could be energetically possible if autoionizing states of Hyd^+ are involved, it remains highly unlikely. The feature is more likely due to residual, imperfectly corrected fortuitous events (*i.e.*, arising from two independent single ionizations; see Section 4.3.1).

4.3.5 Comparison with calculations. The excited states (calculated in Section 3.2) will be labelled with their multiplicity, symmetry and the state number with the given multiplicity and symmetry (see Table 1). For example, 28.41 eV corresponds to the third singlet state of symmetry A′ (^{1}A′ 3).

Electronic collision will doubly ionize the molecule and populate excited states. Each excited state will follow its (complex) relaxation path and will lead to the experimentally observed dissociation. So, the measured thresholds are directly linked to the population of a given excited state at vertical geometry. Fig. 8 shows the comparison between our calculations and the measured thresholds. The thresholds are in the 28.5–30.2 eV range, where fortunately few excited states exist, so are relatively isolated from each other.

The main fragmentation pattern that results in dissociation into $28^+/43^+$ (+29°) corresponds to the ^{1}A′ 4 or ^{3}A′ 3 states. By examining the decomposition of excited states in molecular orbital (MO) configurations, we can imaginatively attribute these states to holes in these MOs. For states ^{1}A′ 4 and ^{3}A′ 3, the holes occur in the (HOMO−1, HOMO−1), (HOMO, HOMO) and (HOMO−4, HOMO) orbitals respectively. The dissociation into $29^+/43^+$ (+28°) could correspond to population of ^{1}A″ 4 which corresponds to a wide distribution on (HOMO−3, HOMO−1), (HOMO−3, HOMO), (HOMO−2, HOMO−1), and (HOMO−3, HOMO−4). For these dissociation channels, as 43^+ is an open shell fragment and a doublet, one of the other fragments must also be a doublet. The combination of spins gives the possibility of an initial singlet or triplet state. In contrast, the $44^+/56^+$ two body dissociation is constituted by two closed shell fragments (in their ground states) and so a singlet initial state should be involved. The ^{1}A′ 3 and ^{1}A″ 3 states, which correspond to (HOMO−1, HOMO), (HOMO, HOMO) and (HOMO−2, HOMO−1), (HOMO−3, HOMO−1), and (HOMO−2, HOMO−4), respectively, are candidates. The energy of the latter (^{1}A″ 3) is closer to the measured threshold.

The difference between energy threshold and corresponding dissociation limit gives an idea about kinetic energy release during the dissociation process.

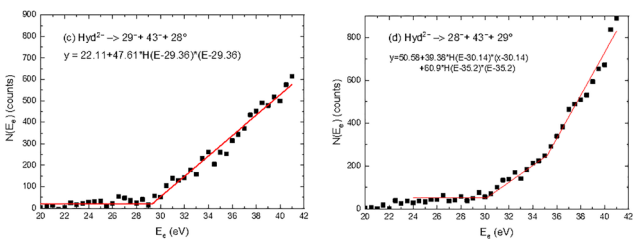

Fig. 7 Intensity evolution of (c) $29^+/43^+$ and (d) $28^+/43^+$ correlations *vs.* electron energy.

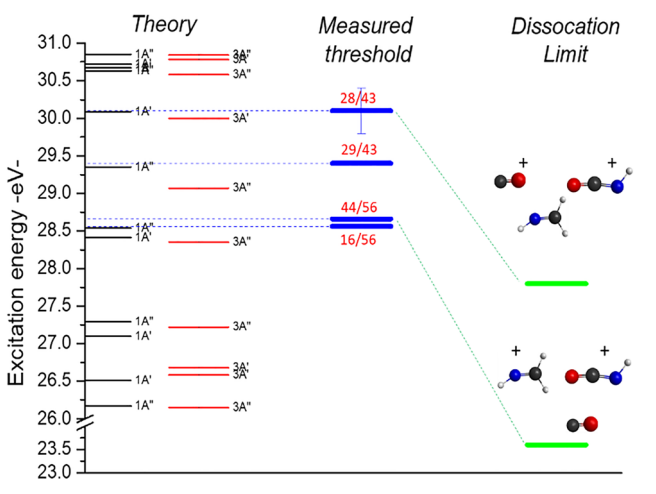

Fig. 8 Comparison between calculated excited states and fragmentation thresholds. Two dissociation limits are given. These correspond to the 'natural' fragments that may be seen in their ground states.

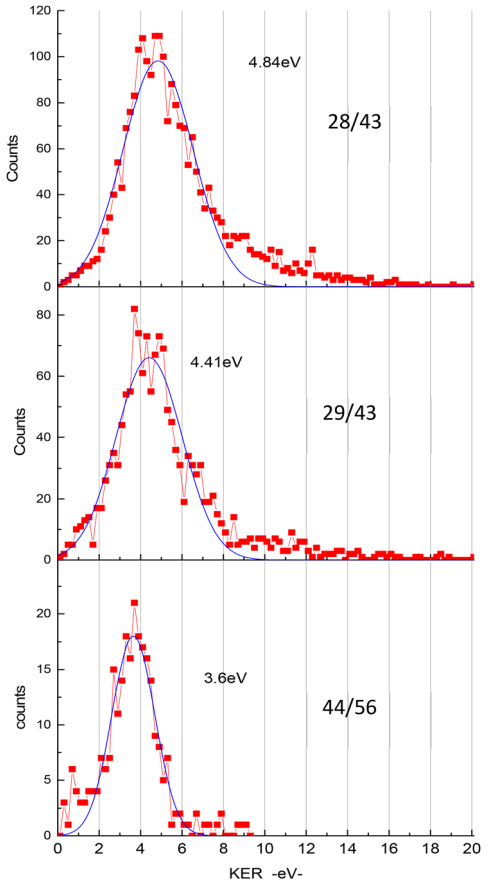

Fig. 9 KER distribution of the major dissociation channels and Gaussian fit.

4.4 Analysis of the kinetic energy released from main dissociation channels

When a doubly charged molecule dissociates into two charged fragments, the coulombic repulsion between the cations is mostly responsible for the few eV recoil kinetic energy of the cations.

Fig. 9 shows the kinetic energy release (KER) distribution of the major channels observed at 40 eV collision energy.

Maxima of the distribution are found at 4.8, 4.4 and 3.6 eV for $28^+/43^+$, $29^+/43^+$ and $44^+/56^+$ correlations, respectively, whereas a crude estimation from the fragmentation threshold and 'simple' dissociation limits (evaluated in Section 4.3.5) gives 2.8 eV and 6.1 eV for $28^+/43^+$ and $29^+/43^+$, respectively. The KER is one signature of the dissociation path. In a pure dissociative energy curve, the KER is the difference between the highest energy of the potential energy surface (PES) reached by an initial Franck–Condon electronic excitation from the neutral molecule and the dissociation energy limit which corresponds to fragments 0 excited electronically or vibrationally. The complexity of analysis of the experimental fragmentation, thanks to the cold supersonic jet, can be seen for the 'simple' diatomic dication CO^{2+} in ref. 30 and the related PES of the two-body fragmentation of CO_2^{2+} into $CO^+ + O^+$.[8]

40 eV collision energy incident electrons have the possibility to populate many excited states, converging to specific dissociation limits (possibly with excited fragments), giving rise to an unresolved KER distribution. Ideally, one would determine the KER distribution at a threshold for fixing one dication excited state (and so one dissociation limit), but the experiment requires a long acquisition time and a very low rate of random correlation. Energy loss and/or zero kinetic energy determination (ZEKE) in correlation could provide more information.

5 Conclusion

In this paper, we presented new results on the fragmentation of hydantoin following double ionisation induced by electronic impact in the 20–40 eV energy range. No unfragmented dication was observed, in contrast to what was observed in keV O^{6+} with hydantoin collisions. The main patterns of fragmentation into two monocations were identified, and the corresponding appearance energies from 28.5–30.5 eV were measured by means of a comprehensive analysis including correction for fortuitous events. Two fragmentation patterns showed unambiguously a hydrogen transfer which has the signature of a hydrogen transfer in excited state mechanism. Investigation of the excited electronic states of doubly ionised hydantoin were carried out by the EOM-DIP-CCSD(3h-1p) method and the stability of the calculations was carefully verified. This allowed us to establish a new vertical double ionisation potential at 26.1 eV. The comparison between theoretical excitation energies and experimental results shows that only a few excited states can be invoked to explain our experimental findings. A study of the dynamic evolution of these particular states will be undertaken in the future. Thanks to the VMI capability of our experimental set-up, we have been able to obtain the KER of the main dissociation at 40 eV collision energy. This opens the possibility for further studies to identify the dissociation limits.

Conflicts of interest

There are no conflicts to declare.

Data availability

Data supporting the conclusions of this study are available upon request (jean-philippe.champeaux@irsamc.ups-tlse.fr).

Acknowledgements

This study has been partially supported through the EUR grant NanoX no. ANR-17-EURE-0009 in the framework of the ''Programme des Investissements d'Avenir''. The authors would like to thank Dr Thomas S. Hearne for a thorough reading of the manuscript.

Notes and references

1 J. P. Champeaux, P. Moretto-Capelle, J. Renoud, L. Polizzi, S. Faure, D. Castex, M. Gianesin, E. Panader, P. Paquier,

W. Volondat, T. Salbaing, J. Riffaud, R. Point, P. Cafarelli and M. Sence, *Phys. Chem. Chem. Phys.*, 2023, **25**, 15497–15507.
2 P. de Marcellus, P. Modica, C. Meinert, L. Nahon, U. I. Meiherhenrich and L. Le Sergeant d'Hendecour, *EPSC Abstracts*, 2014, **9**, 72.
3 P. De Marcellus, M. Bertrand, M. Nuevo, F. Westall and L. Le Sergeant D'Hendecourt, *Astrobiology*, 2011, **11**, 847–854.
4 J. Lilensten, C. Simon Wedlund, M. Barthélémy, R. Thissen, D. Ehrenreich, G. Gronoff and O. Witasse, *Icarus*, 2013, 169–187.
5 P. Franceschi, R. Thissen, J. Žabka, J. Roithová, Z. Herman and O. Dutuit, *Int. J. Mass Spectrom.*, 2003, 507–516.
6 J. Roithová and D. Schröder, *Phys. Chem. Chem. Phys.*, 2007, 2341–2349.
7 H. Hogreve, *J. Phys. B: At., Mol. Opt. Phys.*, 1995, L263.
8 M. Hochlaf, F. R. Bennett, G. Chambaud and P. Rosmus, *J. Phys. B: At., Mol. Opt. Phys.*, 1998, 2163.
9 S. Falcinelli and M. Rosi, *Molecules*, 2020, 4157.
10 J. Renoud, S. Indrajith, A. Domaracka, P. Rousseau, P. Moretto-Capelle, B. A. Huber and J. P. Champeaux, *Phys. Chem. Chem. Phys.*, 2020, 5785–5796.
11 S. X. Tian, *Phys. Chem. Chem. Phys.*, 2012, 6433–6443.
12 T. Masuoka, *Phys. Rev. A: At., Mol., Opt. Phys.*, 1994, 3886.
13 S. Denifl, B. Sonnweber, G. Hanel, P. Scheier and T. D. Märk, *Int. J. Mass Spectrom.*, 2004, 47–53.
14 **https://www.roentdek.com**.
15 **https://www.ismo.universite-paris-saclay.fr/dtpi/**.
16 Z. F. Sun, Z. Farooq, D. H. Parker, P. J. J. Martin and C. M. Western, *J. Phys. Chem. A*, 2019, 6886–6896.
17 G. Sampoll, R. L. Watson, O. Heber, V. Horvat, K. Wohrer and M. Chabot, *Phys. Rev. A: At., Mol., Opt. Phys.*, 1992, 2903–2914.
18 V. Korobov and A. Yelkhovsky, *Phys. Rev. Lett.*, 2001, 193003.
19 M. W. Schmidt, K. K. Baldridge, J. A. Boatz, S. T. Elbert, M. S. Gordon, J. H. Jensen, S. Koseki, N. Matsunaga, K. A. Nguyen, S. Su, T. L. Windus, M. Dupuis and J. A. Montgomery, *J. Comput. Chem.*, 1993, 1347–1363.
20 M. Nooijen and R. J. Bartlett, A new method for excited states: Similarity transformed equation-of-motion coupled-cluster theory, *J. Chem. Phys.*, 1997, 6441–6448.
21 M. Nooijen, *Int. J. Mol. Sci.*, 2002, 656–675.
22 K. W. Sattelmeyer, H. F. Schaefer III and J. F. Stanton, *Chem. Phys. Lett.*, 2003, 42–46.
23 E. Epifanovsky, A. T. B. Gilbert, X. Feng, J. Lee, Y. Mao, N. Mardirossian, P. Pokhilko, A. F. White, M. P. Coons, A. L. Dempwolff, Z. Gan, D. Hait, P. R. Horn, L. D. Jacobson, I. Kaliman, J. Kussmann, A. W. Lange, K. U. Lao, D. S. Levine, J. Liu, S. C. McKenzie, A. F. Morrison, K. D. Nanda, F. Plasser, D. R. Rehn, M. L. Vidal, Z.-Q. You, Y. Zhu, B. Alam, B. J. Albrecht, A. Aldossary, E. Alguire, J. H. Andersen, V. Athavale, D. Barton, K. Begam, A. Behn, N. Bellonzi, Y. A. Bernard, E. J. Berquist, H. G. A. Burton, A. Carreras, K. Carter-Fenk, R. Chakraborty, A. D. Chien, K. D. Closser, V. Cofer-Shabica, S. Dasgupta, M. de Wergifosse, J. Deng, M. Diedenhofen, H. Do, S. Ehlert, P.-T. Fang, S. Fatehi, Q. Feng, T. Friedhoff, J. Gayvert, Q. Ge, G. Gidofalvi, M. Goldey, J. Gomes, C. E. González-Espinoza, S. Gulania, A. O. Gunina, M. W. D. Hanson-Heine, P. H. P. Harbach, A. Hauser, M. F. Herbst, M. Hernández Vera, M. Hodecker, Z. C. Holden, S. Houck, X. Huang, K. Hui, B. C. Huynh, M. Ivanov, Á. Jász, H. Ji, H. Jiang, B. Kaduk, S. Kähler, K. Khistyaev, J. Kim, G. Kis, P. Klunzinger, Z. Koczor-Benda, J. H. Koh, D. Kosenkov, L. Koulias, T. Kowalczyk, C. M. Krauter, K. Kue, A. Kunitsa, T. Kus, I. Ladjánszki, A. Landau, K. V. Lawler, D. Lefrancois, S. Lehtola, R. R. Li, Y.-P. Li, J. Liang, M. Liebenthal, H.-H. Lin, Y.-S. Lin, F. Liu, K.-Y. Liu, M. Loipersberger, A. Luenser, A. Manjanath, P. Manohar, E. Mansoor, S. F. Manzer, S.-P. Mao, A. V. Marenich, T. Markovich, S. Mason, S. A. Maurer, P. F. McLaughlin, M. F. S. J. Menger, J.-M. Mewes, S. A. Mewes, P. Morgante, J. W. Mullinax, K. J. Oosterbaan, G. Paran, A. C. Paul, S. K. Paul, F. Pavošević, Z. Pei, S. Prager, E. I. Proynov, Á. Rák, E. Ramos-Cordoba, B. Rana, A. E. Rask, A. Rettig, R. M. Richard, F. Rob, E. Rossomme, T. Scheele, M. Scheurer, M. Schneider, N. Sergueev, S. M. Sharada, W. Skomorowski, D. W. Small, C. J. Stein, Y.-C. Su, E. J. Sundstrom, Z. Tao, J. Thirman, G. J. Tornai, T. Tsuchimochi, N. M. Tubman, S. P. Veccham, O. Vydrov, J. Wenzel, J. Witte, A. Yamada, K. Yao, S. Yeganeh, S. R. Yost, A. Zech, I. Y. Zhang, X. Zhang, Y. Zhang, D. Zuev, A. Aspuru-Guzik, A. T. Bell, N. A. Besley, K. B. Bravaya, B. R. Brooks, D. Casanova, J.-D. Chai, S. Coriani, C. J. Cramer, G. Cserey, A. E. DePrince III, R. A. DiStasio Jr., A. Dreuw, B. D. Dunietz, T. R. Furlani, W. A. Goddard III, S. Hammes-Schiffer, T. Head-Gordon, W. J. Hehre, C.-P. Hsu, T.-C. Jagau, Y. Jung, A. Klamt, J. Kong, D. S. Lambrecht, W. Liang, N. J. Mayhall, C. W. McCurdy, J. B. Neaton, C. Ochsenfeld, J. A. Parkhill, R. Peverati, V. A. Rassolov, Y. Shao, L. V. Slipchenko, T. Stauch, R. P. Steele, J. E. Subotnik, A. J. W. Thom, A. Tkatchenko, D. G. Truhlar, T. Van Voorhis, T. A. Wesolowski, K. B. Whaley, H. L. Woodcock III, P. M. Zimmerman, S. Faraji, P. M. W. Gill, M. Head-Gordon, J. M. Herbert and A. I. Krylov, *J. Chem. Phys.*, 2021, 084801.
24 T. Kus and A. I. Krylov, *J. Chem. Phys.*, 2012, 244109.
25 A. Marie, P. Romaniello, X. Blase and P.-F. Loos, *J. Chem. Phys.*, 2025, **162**, 134105.
26 J. H. D. Eland, Dynamics of Fragmentation Reactions From Peak Shapes inMultiparticle Coincidence Experiments, *Laser Chem.*, 1991, 259–263.
27 G. H. Wannier, *Phys. Rev.*, 1953, 817.
28 T. Fiegele, G. Hanel, I. Torres, M. Lezius and T. D. Märk, *J. Phys. B: At., Mol. Opt. Phys.*, 2000, 4263.
29 C. Jouvet, M. Miyazaki and M. Fujii, *Chem. Sci.*, 2021, 2836–2856.
30 M. Tarisien, L. Adoui, F. Frémont, D. Lelièvre, L. Guillaume, J. Y. Chesnel, H. Zhang, A. Dubois, D. Mathur, S. Kumar, M. Krishnamurthy and A. Cassimi, *J. Phys. B: At., Mol. Opt. Phys.*, 2000, L11.

